

## Clues to the shapes of very hot nuclei: Calculated patterns for evaporative emission from deformed nuclei

N. N. Ajitanand,<sup>(a),(b)</sup> G. La Rana,<sup>(c)</sup> R. Lacey,<sup>(b)</sup> David J. Moses,<sup>(c)</sup> Louis C. Vaz,<sup>(b)</sup>  
G. F. Peaslee,<sup>(b)</sup> D. M. de Castro Rizzo,<sup>(b)</sup> Morton Kaplan,<sup>(c)</sup> and John M. Alexander<sup>(b)</sup>

<sup>(a)</sup>*Bhabha Atomic Research Centre, Nuclear Physics Division, Trombay 400085, Bombay, India*

<sup>(b)</sup>*Department of Chemistry, State University of New York at Stony Brook, Stony Brook, New York 11794*

<sup>(c)</sup>*Department of Chemistry, Carnegie Mellon University, Pittsburgh, Pennsylvania 15213*

(Received 20 November 1985)

Evaporation-like emission of light particles ( $n$ ,  $H$ ,  $He$ , . . .) has been observed for many nuclear reactions that populate composite nuclei with temperatures of up to  $\approx 5$  MeV and spins as high as  $\approx 150\hbar$ . The measured average energies for the light charged particles are often significantly lower than calculations for evaporation from spherical nuclei. Detailed calculations have not been reported for the role of deformation in evaporative emission patterns, and thus the interpretation of such data has been severely limited. In this paper we describe a method for making evaporation calculations for deformed nuclei, and we present results for several systems with temperatures of 2–5 MeV. The trends of the calculated results are compared to those for spherical emitters in order to get a feeling for those effects peculiar to the deformations. The patterns of calculated spectra and angular distributions encourage the notion that such studies can give valuable clues to the shapes of these very hot nuclei.

### I. INTRODUCTION

In most discussions of reactions between complex nuclei, one divides the various degrees of freedom into those of the intrinsic particles and those of collective motions, such as the shape of the surface.<sup>1</sup> A typical schematic diagram of the evolution of nuclear shapes during a heavy-ion reaction is shown in Fig. 1. First, one conceives of two nearly spherical and cold reactant nuclei being hurled at one another to form a dinuclear system. Depending on the balance between nuclear attractions and Coulomb and centrifugal repulsions, this dinuclear system may break up (e.g., quasielastic or deeply inelastic collisions, fragmentation, etc.) or it may develop a neck and fuse<sup>2</sup> into, for example, a pear-shaped or even more symmetric spheroidal object.

While these collective motions are occurring, the intrinsic nuclear particles are, of course, undergoing individual collisions and transfers between regions originally identified with the target or projectile.<sup>3</sup> The individual particles are being driven toward thermal equilibrium<sup>4</sup> while, during the same period, the nuclear surface is being driven toward its equilibrium shape.<sup>5</sup> The relative rates of these two kinds of relaxation are not well known. Some treatments have assumed that shape equilibration essentially always proceeds thermalization,<sup>6</sup> while others feel that thermalization takes place much more rapidly than the collective movements of the nuclear surface.<sup>7</sup>

The liquid drop model, in its various forms, has provided very clear guidance for nuclear forms after shape equilibration,<sup>5</sup> but it is much more difficult to determine the time necessary to achieve such shape equilibrium.<sup>2,3,8</sup> The intuitive feeling of many is that shape equilibrium may well be achieved rather often in nuclear reactions in-

volving reasonably low nuclear charge, incident energy, and angular momentum. By contrast, it is the dynamical shape evolution that is of major concern for high charge, energy, and/or angular momentum, as there are no equilibrium nuclear shapes<sup>2–5</sup> (these systems are unstable with respect to fission).

The statistical model for nuclear evaporation provides very clear guidance for the energy and angular distributions of light particles emitted from a composite system

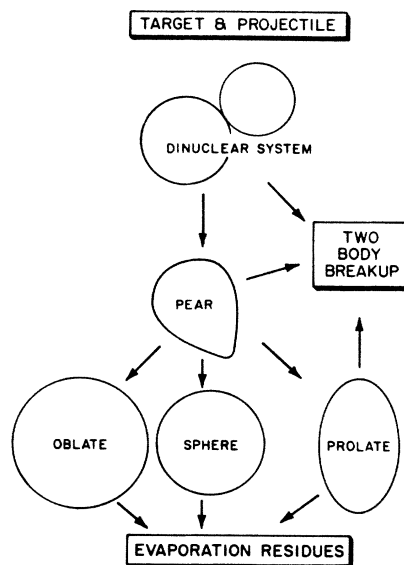


FIG. 1. Schematic diagram of a possible evolution of nuclear shapes from the target-projectile entrance channel to two-body breakup or evaporation residues.

after energy thermalization.<sup>9</sup> Our understanding of the preequilibrium emission of light particles is in a much more primitive stage of development.<sup>10</sup> Experimental studies of the energy and angular distributions of light particles generally indicate quite an abundance of evaporation-like emission.<sup>11</sup> This evaporative emission seems to occur both in route to evaporation residues and prior to two-body breakup reactions.

The thermalized, emitting nuclei could conceivably be identified with any of the forms in Fig. 1. It would be very interesting to determine the properties of these very hot nuclei before the cooling that results from a long cascade of emitted particles, fission-like fragments, and  $\gamma$  rays. Most of the  $\gamma$ -ray emission takes place towards the end of this cascade and, therefore,  $\gamma$ -ray studies give information primarily on relatively cool nuclei. Nuclear fission can occur from the hot, stretched-out nuclei and, therefore, fission-fragment studies give information on those particular nuclear systems in transition from saddle-to scission-point configurations.<sup>12</sup> Evaporative particle emission begins to occur just after energy thermalization, and therefore, studies of these particles can give information on the very hot nuclei (either before or after fission-like breakup or for nonfissile nuclei).

Evaporative spectra and angular distributions are determined by the spin, excitation energy, and potential barrier of the emitter, as well as by the level density at the "transition-state" configuration.<sup>9,12</sup> The effective size and shape of this transition-state system are intimately related to its potential barrier, moment of inertia, and temperature (especially for charged particles).<sup>13,14</sup> Therefore, it is possible to search for clues concerning these nuclear sizes and shapes by detailed analysis of observed angular and energy distributions of the evaporated particles. Our focus in this study is on the role of the nuclear shapes and the associated anisotropic effects that can be expected. A kind of scaling of these effects can be expected to result from alterations in the size of the emitting system.

The equilibrium statistical model has been very well developed for the case of emission from spherical nuclei.<sup>9</sup> By contrast, for deformed nuclei only crude calculations have been published for rather special situations (e.g.,  $s$ -wave emission, emission from the tips of a prolate nucleus, etc.). In this paper we pursue a much more consistent treatment of evaporation from deformed nuclei. We use the Cassini shape parametrization as described by Pashkevich,<sup>14</sup> and semiclassical methods as discussed by Ericson,<sup>9</sup> Dossing,<sup>15</sup> and others.<sup>11</sup> We follow the signposts in Ref. 15, but since the required integrations are not well suited for analytic methods (various nuclear orientations, surface positions, exit-channel  $l$  values, etc.), we employ Monte Carlo techniques in the framework of the well-documented computer code GANES.<sup>16</sup>

Our purpose in this paper is to describe the method and to show how certain observable properties (e.g., mean energies and angular anisotropies) are predicted to vary with the shape of the emitter. We compare calculated emission patterns from prolate, oblate, pear-shaped, and spherical nuclei for several cases. The results of these calculations encourage the notion that evaporation spectra for light charged particles can indeed give meaningful clues to the

shapes of very hot nuclei. Comparisons to experimental results will be made in subsequent papers in which the properties of the individual reaction processes can be discussed in more detail.<sup>17</sup>

## II. AN OVERVIEW OF THE PROBLEM AND OUR APPROACH

The basic task of an evaporation model is the formulation of the relative probability  $S_{E_0, J_0}(\epsilon, l, \phi)$  for emission of a light particle with channel energy  $\epsilon$  and orbital angular momentum  $l$  at an angle  $\phi$  with respect to the spin  $J_0$  of a parent nucleus of total excitation energy  $E_0$ . This probability is taken as the product of a transmission coefficient  $T_l$  (that contains the dynamical information) and a level density  $\rho$  (or number of open channels) at the "effective transition-state" configuration<sup>9,12,15</sup>

$$S_{E_0, J_0}(\phi, \epsilon) \propto \int \int \tilde{T}_l(\epsilon) \rho_d(E_d, \mathbf{J}_d) d\tilde{l} d\phi_l. \quad (1)$$

We use  $\phi_l$  to denote the azimuthal angle for  $l$  (in the plane perpendicular to the emission direction) and we follow the semiclassical approximation of integration over  $\tilde{l}$ , where  $\tilde{l} = l + \frac{1}{2}$ . Acceptable values of  $\mathbf{J}_d$  are constrained by the classical condition that  $l$  be perpendicular to the direction of emission. The relevant level density can be assumed to be that of the daughter nucleus (subscript  $d$ ) at the instant of particle emission. For first step emission from a compound nucleus, the total excitation energy of the parent nucleus is given by

$$E_0 = E_{c.m.} + Q, \quad (2)$$

and the total excitation energy and spin of the daughter nucleus are given by

$$E_d = E_0 - E_s - \epsilon, \quad (3)$$

where  $E_s$  is the particle separation energy and

$$\mathbf{J}_d = \mathbf{J}_0 - \mathbf{l} \quad \text{or} \quad J_d^2 = J_0^2 + l^2 - J_0 l \cos \chi_l, \quad (4)$$

where  $\chi_l$  is the angle between  $\mathbf{J}_0$  and  $\mathbf{l}$ . The level density of the daughter nucleus is usually taken to be that for a Fermi gas,

$$\rho_d(E_d, \mathbf{J}_d) \propto \exp(2\sqrt{aU}) \simeq \rho_d(E_d, 0) \exp(-E_{\text{rot}}/T), \quad (5)$$

with thermal energy  $U$  and temperature  $T$  given by

$$U = E_d - E_{\text{rot}} \simeq aT^2. \quad (6)$$

The transmission coefficient in Eq. (1) is determined by the height and width of the barrier as seen by the emitted particle. For a spherical nuclear system (but not for a deformed one) the value of  $T_l(\epsilon)$  is independent of the azimuthal angle  $\phi_l$ ; hence, for a given emission angle a straightforward integration over this azimuthal angle gives the result<sup>18</sup>

$$S_{E_0, J_0}(\epsilon, \phi) \propto \int_0^\infty \tilde{T}_l(\epsilon) \rho_d(E_d, 0) \exp \left[ -\frac{\hbar^2(\tilde{J}_0^2 + \tilde{l}^2)}{2\mathcal{I}_d T} \right] \times I_0(2\beta_1 \sin \phi) d\tilde{l}. \quad (7)$$

In the above expression the quantity  $\beta_1$  is related to the magnitude of  $\tilde{l}$ , the spin of the parent ( $\tilde{J}_0 = J_0 + \frac{1}{2}$ ), the temperature, and the moment of inertia  $\mathcal{I}_d$  of the daughter,

$$\beta_1 = \hbar^2 \tilde{J}_0 \tilde{l} / 2 \mathcal{I}_d T. \quad (8)$$

For a deformed nucleus the situation is much more complex, as shown in Fig. 2, because the effective emission barrier, as seen by the particle, depends on its point of emission on the nuclear surface. In other words,  $T_l(\epsilon)$  is also a function of  $\chi_l$ , as shown in Fig. 2. Furthermore, for each emission direction  $\phi$ , this emission point (or birthplace) will also depend on the orientation angles ( $\phi^*$  and  $\chi$ ) of the nuclear symmetry axis. Hence we must return to the integrand of Eq. (1) and find a way to make the integrations over these orientation angles. The implicit integrations over  $\phi^*$  and  $\chi$  must be addressed along with the explicit integrations over  $\tilde{l}$  and  $\phi_l$ . For this purpose we have used a Monte Carlo method that involves random samplings of the angles  $\phi^*$ ,  $\chi$ , and  $\phi_l$ , as well as for the other variables  $\tilde{l}$  and  $\epsilon$ .

The calculational framework has been provided by the code GANES,<sup>16</sup> for which we have constructed a special version to consider deformed nuclei. This code employs the weighted Monte Carlo method in which the variables (e.g.,  $\phi^*$ ,  $\chi$ ,  $\phi_l$ ,  $l$ , etc.) are uniformly sampled and a particular weight is assigned for each chosen event.<sup>19</sup> Efficient use of computer time is ensured by considering in detail only those events that involve particle registration in a given detector at a given position. In this paper we will consider ideal coincidence (or singles) experiments that employ small detectors placed at various angles  $\phi$  with

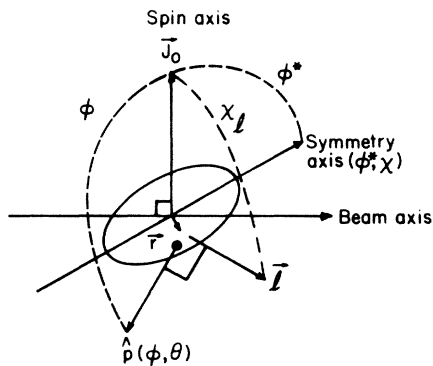


FIG. 2. Geometry for particle evaporation from a deformed nucleus. Particle direction  $\hat{p}$  at polar angle  $\phi$  with respect to the initial spin  $J_0$  and  $\theta$  with respect to the beam. Exit channel orbital angular momentum  $l$  at polar angle  $\chi_l$  with respect to  $J_0$ . Nuclear symmetry axis at angle  $\phi^*$  with respect to  $J_0$  and azimuthal angle (lighthouse angle)  $\chi$  with respect to plane of  $J_0$  and  $\hat{p}$ . The finite impact parameter  $r$  satisfies the relationship  $l = r \times \hat{p}$ , but its magnitude can be neglected for the angle definitions. The solid spot represents the exit point of the particle from the nuclear surface. Note that  $l$  is perpendicular to  $\hat{p}$ , and its azimuthal angle  $\phi_l$  (not included) is measured in the plane perpendicular to  $\hat{p}$ .

respect to the initial spin  $J_0$  (or  $\theta$  with respect to the beam axis).

In brief, for a given parent nucleus ( $E_0, J_0$ ) and detector angle ( $\phi$  or  $\theta$ ), we randomly select values for  $\phi^*$ ,  $\chi$ ,  $\phi_l$ ,  $l$ , and  $\epsilon$ . Then we follow the time-reversed trajectory of the particle from detector to impact with the daughter nucleus. We use the potential (Coulomb plus nuclear plus centrifugal) of the deformed nucleus<sup>14</sup> to calculate the transmission coefficient ( $T_l$ ), and we use the inertial parameters ( $\mathcal{I}_{\parallel}$  and  $\mathcal{I}_{\perp}$ ) (Ref. 20) to calculate its rotational energy ( $E_{\text{rot}}$ ), a necessary ingredient for the level density [Eqs. (5) and (6)]. The product  $\tilde{l} T_l \rho$  is proportional to the relative probability or “spectral weight” for that event [Eq. (1)]; its value is stored and the procedure is repeated for a large number of events. (The program also handles a number of important details, such as transformation from emitter to laboratory frame, detector geometries and thresholds, coincidence requirements, recoil effects, etc.) For simplicity we consider here only the c.m. channel-energy spectra for certain ideal situations. In the next section we describe the shape parametrization used and the associated potential energies.

### III. SHAPE PARAMETRIZATION, ASSOCIATED POTENTIAL ENERGIES, AND MOMENTS OF INERTIA

The Cassinian system of orthogonal coordinates ( $R, x$ ) provides a convenient basis for describing a family of shapes that is very useful for nuclear physics.<sup>14</sup> A Cassinian coordinate grid can be related to ordinary cylindrical coordinates ( $r, z$ ) as follows:

$$R = [(z^2 + r^2)^2 - 2s(z^2 - r^2) + s^2]^{1/4}, \quad (9)$$

$$x = \frac{\text{sgnz}}{\sqrt{2}} \left\{ 1 + \frac{(z^2 - r^2 - s)}{[(z^2 + r^2)^2 - 2s(z^2 - r^2) + s^2]^{1/2}} \right\}^{1/2}, \quad (10)$$

where the scaling parameter  $s$  is the square of the distance from the focus of the Cassinian ovals to the coordinate origin. For example, by using only one parameter  $\tilde{\epsilon}$  ( $s = \tilde{\epsilon} R_0^2$ , where  $R_0$  is the equivalent spherical radius), one may specify an extensive series of shapes, some of which are shown in Fig. 3. After axial rotation these shapes (scaled to constant volume) range from spherical ( $\tilde{\epsilon} = 0$ ) to barely touching deformed fragments ( $\tilde{\epsilon} = 1.0$ ) to completely separated fragments of equal size ( $\tilde{\epsilon} > 1.0$ ). For  $0 < \tilde{\epsilon} < 0.5$  the shapes are nearly prolate spheroids with an axis ratio  $d_1/d_2$  of

$$d_1/d_2 \approx (1 + \frac{2}{3}\tilde{\epsilon}) / (1 - \frac{2}{3}\tilde{\epsilon}). \quad (11)$$

Similarly, for  $-0.5 < \tilde{\epsilon} < 0$  the shapes generated (not shown in Fig. 3) are nearly oblate spheroids, also with the axis ratio of Eq. (11). For  $0.5 < \tilde{\epsilon} < 1.0$  the shapes exhibit a “neck” between two “droplets” of equal size, as indicated in Fig. 3.

It is also straightforward to generate shapes that are asymmetric to reflection by a plane perpendicular to the symmetry axis. To this end a “dipole” perturbation can be introduced as follows, via the parameter  $\alpha_1$ :

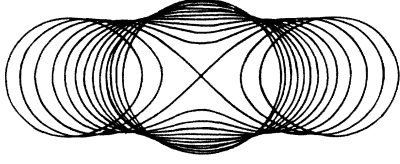


FIG. 3. Cassinian ovals are a single-parameter family of curves convenient for use in approximating the nuclear surface shape. The volume is conserved in this figure. The parameter  $\tilde{\epsilon}$  varies from 0 (sphere) to 1.2 with steps of 0.1 ( $\tilde{\epsilon}=1.1$  and 1.2 correspond to separated fragments). At  $\tilde{\epsilon}=1.0$  (Bernoulli lemniscate) the curve has a double point at the center of symmetry (after Ref. 14).

$$R(x) = R_0[1 + \alpha_1 P_1(x)], \quad (12)$$

where  $P_1(x)$  is the first order Legendre polynomial. Examples of such perturbed shapes are shown in Fig. 4. Thus with only two parameters ( $\tilde{\epsilon}$  and  $\alpha_1$ ), and the condition of volume conservation, one may represent a rather extensive range of axially symmetric shapes.

The exact form of the Coulomb potential for such nuclei has been given in Ref. 14, in terms of elliptic integrals. Similarly, the nuclear potential has been represented as an extension of the Woods-Saxon form for a spherical nucleus,

$$V = V_0[1 + \exp(\psi/\tilde{a})]^{-1}, \quad (13)$$

where  $\psi$  is the approximate distance between a point and the nuclear surface, and  $V_0$  and  $\tilde{a}$  are the conventional well depth and diffusivity parameters.<sup>14</sup> In our calculations the well depth  $V_0$  is taken to be 127 MeV,<sup>20</sup> and the diffusivity  $\tilde{a}$  is chosen to reproduce empirical fusion barriers between cold nuclei<sup>21</sup> ( $\tilde{a} \approx 0.8$  fm). Exact relations for the moments of inertia  $\mathcal{I}_{\parallel}$  and  $\mathcal{I}_{\perp}$  (parallel and perpendicular to the axis) are given in Ref. 20. (We use a radius constant of 1.2 fm for the matter distribution.<sup>5,14</sup>)

#### IV. OUTLINE OF THE CALCULATION

For simplicity we will consider an ensemble of  $N_t$  emitting nuclei, each with the same initial excitation energy  $E_0$  and spin  $J_0$ . We calculate the energy spectrum for  $^4\text{He}$  particles in two situations: (1) an ideal coincidence

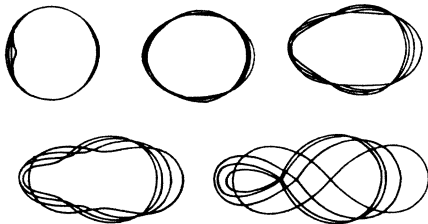


FIG. 4. Cassinian ovals perturbed by "dipole" ( $\alpha_1 \neq 0$ ) deformation.  $\alpha(\tilde{\epsilon})=0.0, 0.25,$  and  $0.50$  correspond to the figures in the upper row,  $\alpha(\tilde{\epsilon})=0.75$  and  $1.00$  to the lower row. (See Eq. 10 in Ref. 14.) In each figure, the curves correspond to  $\alpha_1=0.0, 0.1, 0.2,$  and  $0.3$  (after Ref. 14).

experiment for which the spin vector is parallel to the  $y$  axis ( $M=J_0$ ), and (2) an ideal singles experiment for which the spin vectors are uniformly oriented in the  $xy$  plane ( $M=0$ ) perpendicular to the beam (or  $z$ ) axis. For each emitter we use the integrand of Eq. (1) to calculate the probability for emission  $(\tilde{I}T_1\rho_d)_k$  that leads to detection of a particle with channel energy  $\epsilon$  at a certain angle  $\phi$  with respect to  $J_0$  (or  $\theta$  with respect to the beam). To effect the integration [analogous to that in Eq. (1)], we bin and sum these probabilities or weights as follows:

$$N(\epsilon, \hat{p}) = \left[ \frac{1}{N_t} \right] \sum_{k=1}^{N_t} (\tilde{I}T_1\rho_d)_k \tilde{P}_k(\phi^*), \quad (14)$$

where the direction of the particle detector is denoted by  $\hat{p}$ . The probability for each value of  $\phi^*$  is taken from the Boltzmann factor

$$\begin{aligned} \tilde{P}_k(\phi^*) &\propto \exp(-\tilde{E}_{\text{rot}}/T) \\ &\propto \exp[-(\hbar J_0 \cos \phi^*)^2 (\mathcal{I}_{\perp} - \mathcal{I}_{\parallel}) / 2\mathcal{I}_{\parallel} \mathcal{I}_{\perp} T] \end{aligned}$$

for the parent nucleus.<sup>12</sup> (Note that for prolate shapes  $\mathcal{I}_{\perp} > \mathcal{I}_{\parallel}$  and  $\phi^* = 90^\circ$  is preferred, while for oblate shapes  $\mathcal{I}_{\parallel} > \mathcal{I}_{\perp}$  and  $\phi^* = 0^\circ$  is preferred.)

Figure 5 shows an outline of the calculational procedure. (1) The first task is to obtain a potential energy map for the emitted particle from the equations given in Refs. 14 and 20. This map, as well as the moments of inertia for the deformed nucleus, are then stored and used for each individual calculation. (2) Then, for each event, specific values are selected, by means of random numbers, for each variable ( $J_0, \epsilon, l, \phi^*, \chi,$  and  $\phi_l$ ) shown in Fig. 2. These selections are made *uniformly* over a range of sufficient size to include any significant probability of oc-

#### CALCULATIONAL PROCEDURE for Emitter ( $E_0, J_0$ ) with Deformation ( $\tilde{\epsilon}, \alpha,$ )

1. Map Potential between Particle & Deformed Nucleus

Then For Each Event

2. Choose by Random Selection
  - Initial Spin  $J_0$
  - Exit Channel  $\epsilon$  and  $l$
  - Orientation of Nuclear Symmetry Axis  $\phi^*, \chi$
  - Direction of  $l$  Vector,  $\phi_l$
3. Follow Particle Trajectory from Detector to Impact Point on the Nuclear Surface
4. Calculate Potential Barrier ( $B, R$ ) and Transmission Coefficient,  $T_l$
5. Calculate Level Density of the Residual Nucleus,  $\rho_d$
6. Add the Weight  $(\tilde{I}T_1\rho_d \tilde{P}(\phi^*))_k$  to Bins for the Desired Spectra

Repeat Steps 2-6 for Many Events to Obtain a Sufficient Sample

FIG. 5. Outline of the calculational procedure. More detail concerning the program GANES and the weighted Monte Carlo method is given in Ref. 16.

currence.<sup>16</sup> (Note that our choice of independent variables, particularly  $\phi_l$ , differs from those in Ref. 18. These variables lead to an equivalent description but are much more convenient in this context.) (3) Next we determine the time-reversed trajectory of the emitted particle so as to fix its exit (or impact) point, and (4) calculate its transmission coefficient.<sup>15</sup> (5) From the conservation laws [Eqs. (3) and (4)] we determine the excitation energy and spin of the daughter ( $E_d, J_d$ ), its rotational energy  $E_{\text{rot}}$  ( $K$  denotes the projection of  $J_d$  on the symmetry axis),

$$E_{\text{rot}} = \frac{\hbar^2}{2} \left[ \frac{J_d^2 - K^2}{\mathcal{I}_\perp} + \frac{K^2}{\mathcal{I}_\parallel} \right], \quad (15)$$

and its level density from Eqs. (2)–(6). The nuclear symmetry axis is held fixed in space during particle emission, but the spin axis is altered according to Eq. (4). [Note that the probability weighting for  $\phi^*$  is determined by  $P(\phi^*)$  above; the role of  $K$  in Eq. (15) is related to the weighting of  $\hat{p}$  and  $l$  for the emitted particle.] (6) Finally, we add the weight for this event to the appropriate bin for the desired energy spectrum. This weighted Monte Carlo integration process<sup>16,19</sup> is then repeated until all the variables have been adequately sampled.

For the particular results that are reported here, we have assumed that the lifetime of the emitter is greater than the rotation time. Hence, each value of the azimuthal angle  $\chi$  is equally likely. In addition, we have used hyperbolic Rutherford trajectories, assuming that they give a reasonable representation of the distribution of the impact points (or birthplaces) on the surface of these deformed, but randomly oriented, nuclei.<sup>15</sup> For the transmission coefficients we use the particular potential energy curve for the normal to the nuclear surface at the impact point. Two separate parabolas are fitted to the inner and outer curvatures ( $\hbar\omega_i$  and  $\hbar\omega_o$ ) of the potential at the barrier maximum ( $B, R$ ). Then the value of  $T_l(\epsilon)$  is calculated from the modified Hill-Wheeler<sup>22</sup> formula,

$$T_l(\epsilon) = (1 + e^x)^{-1}, \quad (16)$$

where

$$x = \left[ B - \epsilon + \frac{\hbar^2 \bar{l}^2}{2\mu R^2} \right] \left[ \frac{2\pi}{\hbar\omega_{\text{eff}}} \right] \quad (17)$$

and

$$\frac{1}{\hbar\omega_{\text{eff}}} = \frac{1}{2} \left[ \frac{1}{\hbar\omega_i} + \frac{1}{\hbar\omega_o} \right]. \quad (18)$$

In this equation,  $B$  is the effective  $s$ -wave barrier and  $\mu$  is the reduced mass.

This framework provides a simple means of describing evaporative emission from a deformed nucleus with explicit consideration of each of the important variables. The method is semiclassical, and thus one must be alert in each case to the possible role of specific wave mechanical properties. Typically, the wave properties are effectively averaged out if the number of important  $l$  waves is sufficient, and if  $J_0 > l$ . A test of this point has been made by semiclassical and quantum mechanical calculations for spherical emitters.<sup>23</sup> The differences between these two

formulations for several typical systems are very small indeed.

In the present calculations we have employed certain approximations to simplify the description: (a) Rutherford trajectories, (b) Hill-Wheeler penetrabilities, and (c) simplified level density formulation. None of these approximations is essential to the treatment, and, in fact, we plan to remove several of them. Nevertheless, we feel that the present treatment is more than adequate to demonstrate the qualitative (and even semiquantitative) role of shape changes on evaporative particle emission. Furthermore, we feel that this kind of Monte Carlo method is both easy to employ and quite simple for maintaining identity and control of the various features of the physical model. The multistep evaporation codes that are already in use often involve rather complex structures that are less amenable to the addition of new features such as nuclear deformation, the geometric constraints inherent in angular distribution studies for various coincidence modes, etc. Our approach, as embodied in the GANES program,<sup>16</sup> is modular and flexible both in concept and in execution. It also can provide results in the laboratory system even when the reaction kinematics, recoil effects, etc. are complex. This aspect is very important, especially if several emission sources are present.

## V. ANALYTICAL EQUATIONS FOR SPHERICAL NUCLEI

It is very useful to consider the case of spherical emitters before examining the results for deformed systems. For the special case of sharp cutoff transmission coefficients,

$$\begin{aligned} T_l &= 0 \quad \text{for } \epsilon < B + \hbar^2 \bar{l}^2 / 2\mu R^2, \\ T_l &= 1 \quad \text{for } \epsilon \geq B + \hbar^2 \bar{l}^2 / 2\mu R^2, \end{aligned} \quad (19)$$

one may integrate Eq. (1) analytically (over  $\phi_l, \bar{l}$ , and  $\epsilon$ ) to obtain the following equations:<sup>9,11,15,18,23–25</sup>

$$S_{E_0, J_0}(\phi) \propto \exp(\beta_2 \sin^2 \phi). \quad (20)$$

The anisotropy parameter is given by

$$\beta_2 = \frac{\hbar^2 (J_0 + \frac{1}{2})^2}{2\mathcal{I}_d T} \left[ \frac{\mu R^2}{\mathcal{I}_d + \mu R^2} \right]. \quad (21)$$

The average of the square of the exit channel orbital angular momentum  $\langle \bar{l}^2 \rangle$  and the average exit channel energy  $\langle \epsilon \rangle$  may be obtained in the same spirit by using the integrand of Eq. (1) as a weighting function. We have

$$\langle \bar{l}^2 \rangle_\phi = \left[ \frac{2\mu R^2}{\hbar^2} \right] \left[ \frac{\mathcal{I}_d}{\mathcal{I}_d + \mu R^2} \right] T (1 + \beta_2 \sin^2 \phi) \quad (22)$$

$$= \left[ \frac{2\mu R^2}{\hbar^2} \right] \left[ \frac{\mathcal{I}_d}{\mathcal{I}_d + \mu R^2} \right] T + \langle \bar{l}^2 \rangle_{\text{spinoff}} \quad (23)$$

and

$$\langle \epsilon \rangle_\phi = B + T + T \left[ \frac{\mathcal{I}_d}{\mathcal{I}_d + \mu R^2} \right] (1 + \beta_2 \sin^2 \phi), \quad (24)$$

$$\langle \epsilon \rangle_\phi = B + T + \left[ \frac{\hbar^2}{2\mu R^2} \right] \langle \tilde{I}^2 \rangle_\phi \quad (25)$$

$$= B + T + T \left[ \frac{\mathcal{I}_d}{\mathcal{I}_d + \mu R^2} \right] + \langle \epsilon \rangle_{\text{spinoff}}, \quad (26)$$

where

$$\begin{aligned} \langle \epsilon \rangle_{\text{spinoff}} &= \left[ \frac{\hbar^2}{2\mu R^2} \right] \langle \tilde{I}^2 \rangle_{\text{spinoff}} \\ &= \beta_2 \left[ \frac{\mathcal{I}_d}{\mathcal{I}_d + \mu R^2} \right] T \sin^2 \phi. \end{aligned} \quad (27)$$

The anisotropy parameter  $\beta_2$  controls the angular dependence of the emission probability [Eq. (20)], the average of  $\tilde{I}^2$  [Eqs. (22) and (23)], and the average energy [Eqs. (24)–(27)]. There is a component of  $\langle \tilde{I}^2 \rangle$  that is spin dependent (through  $\beta_2$ ), and another component that arises from thermal motion alone [Eq. (23)]. The average energy  $\langle \epsilon \rangle_\phi$  has components derived from three driving forces: the emission barrier  $B$ , the temperature  $T$ , and the spin [through  $\beta_2$  in Eq. (27)]. The component of the mean energy that is driven by angular momentum is called the spinoff energy [Eq. (27)]. Its value has a maximum at  $90^\circ$  to the spin and is zero along the spin axis. The overall pattern of these emission energies will differ strongly depending on the relative magnitudes of  $B$ ,  $T$ , and  $\beta_2$ .

A similar set of equations can be derived for an ideal singles experiment ( $M=0$ ). Here one must average over all orientations of the spin axis in the plane perpendicular to the beam. (We use double angular brackets to indicate this averaging.) In this case the relevant angle ( $\theta$ ) is measured with respect to the beam direction. Here we have, for the relative probability  $W_{E_0, J_0}(\theta)$ ,

$$W_{E_0, J_0}(\theta) \propto \exp\left(-\frac{1}{2}\beta_2 \sin^2 \theta\right) I_0\left(\frac{1}{2}\beta_2 \sin^2 \theta\right), \quad (28)$$

and for the average of  $\tilde{I}^2$ ,

$$\begin{aligned} \langle\langle \tilde{I}^2 \rangle\rangle_\theta &= \left[ \frac{2\mu R^2}{\hbar^2} \right] T \left[ \frac{\mathcal{I}_d}{\mathcal{I}_d + \mu R^2} \right] \\ &\times \left\{ 1 + \beta_2 \cos^2 \theta \right. \\ &\left. + \frac{1}{2}\beta_2 \sin^2 \theta \left[ 1 + \frac{I_1\left(\frac{1}{2}\beta_2 \sin^2 \theta\right)}{I_0\left(\frac{1}{2}\beta_2 \sin^2 \theta\right)} \right] \right\}, \end{aligned} \quad (29)$$

and, finally, for the average of  $\epsilon$ ,

$$\langle\langle \epsilon \rangle\rangle_\theta = B + T + \left[ \frac{\hbar^2}{2\mu R^2} \right] \langle\langle \tilde{I}^2 \rangle\rangle_\theta. \quad (30)$$

Bessel functions of the first kind (of imaginary argument) are denoted by  $I_0$  and  $I_1$ . For the case of  $M=0$  (ideal singles), all the same effects are present that were mentioned above for  $M=J$  (ideal coincidence). However, the averaging over all directions for the emitter spin strongly reduces the angular dependences.

The trends of the calculated results for deformed emitters can be much better understood by reference to these analytical results for spherical emitters.

## VI. CALCULATED RESULTS FOR SOME TYPICAL CASES

The emission patterns for deformed systems respond to the same three driving forces discussed above: the emission barrier  $B$ , the temperature  $T$ , and the spin (or, effectively,  $\beta_2$ ). In this situation, however, each of these driving forces also depends on the shape of the deformed nucleus. We have prepared several figures to illustrate the interplay between these driving forces for reaction systems which are currently being studied experimentally. In this section we emphasize the trends of the calculated results; comparisons to experimental data will be made elsewhere.

In Figs. 6 and 7 we show, for fixed shape, the effect of spin on the anisotropy  $W(90^\circ)/W(0^\circ)$  and on the average quantities  $\langle \epsilon \rangle$  and  $\langle \tilde{I}^2 \rangle^{1/2}$  or  $\tilde{I}_{\text{rms}}$  for  $\phi=0^\circ$  and  $90^\circ$ . To dramatize the role of deformation (and the associated emission barriers), we have made one series of calculations with  $\phi^*$  fixed at  $90^\circ$  for the prolate shape and  $\phi^*=0^\circ$  for the oblate shape. These results are shown in Fig. 6. For zero spin the changes between  $\phi=0^\circ$  and  $\phi=90^\circ$  arise sole-

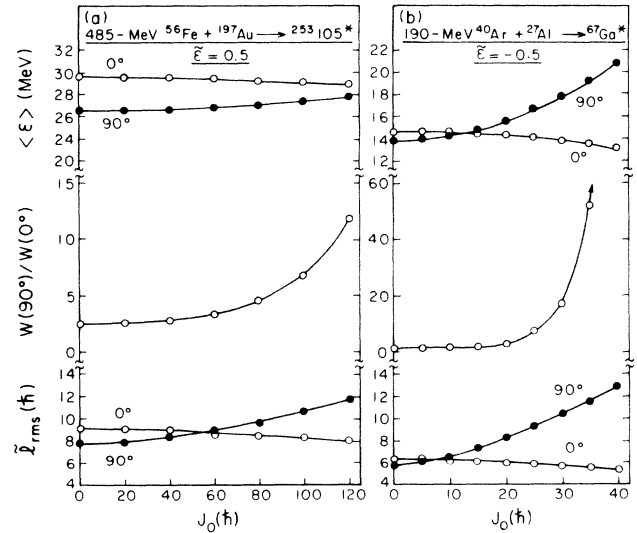


FIG. 6. Dependence on emitter spin  $J_0$  for certain average quantities  $\langle \epsilon \rangle$ ,  $W(90^\circ)/W(0^\circ)$ , and  $\tilde{I}_{\text{rms}}$ . (a) 485 MeV  $^{56}\text{Fe} + ^{197}\text{Au} \rightarrow ^{253}\text{105}^*$  ( $T=2.4$  MeV,  $\tilde{\epsilon} = +0.5$  prolate). (b) 190 MeV  $^{40}\text{Ar} + ^{27}\text{Al} \rightarrow ^{67}\text{Ga}^*$  ( $T=2.9$  MeV,  $\tilde{\epsilon} = -0.5$  oblate). In these cases the orientation of the symmetry axis was frozen at  $90^\circ$  to the spin (i.e.,  $\phi^* = 90^\circ$  for prolate,  $\phi^* = 0^\circ$  for oblate).

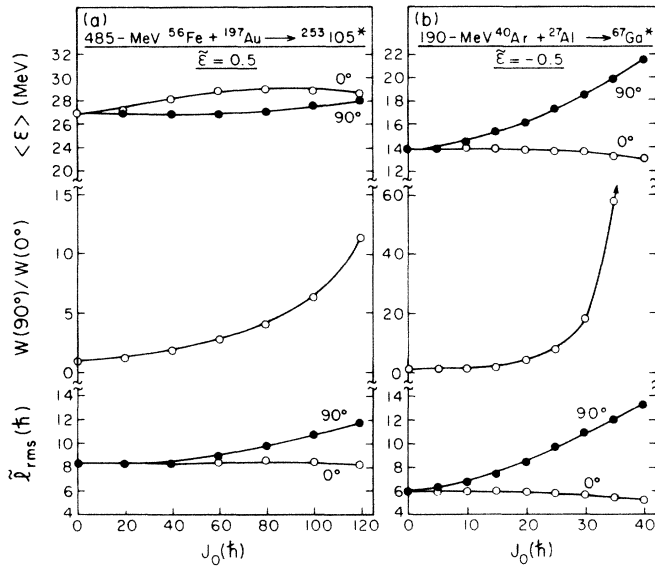


FIG. 7. Dependence on emitter spin  $J_0$  for certain average quantities  $\langle \epsilon \rangle$ ,  $W(90^\circ)/W(0^\circ)$ , and  $\tilde{l}_{rms}$ . (a) 485 MeV  $^{56}\text{Fe} + ^{197}\text{Au} \rightarrow ^{253}105^*$  ( $T=2.4$  MeV,  $\tilde{\epsilon} = +0.5$  prolate). (b) 190 MeV  $^{40}\text{Ar} + ^{27}\text{Al} \rightarrow ^{67}\text{Ga}^*$  ( $T=2.9$  MeV,  $\tilde{\epsilon} = -0.5$  oblate). In these cases the orientation of the symmetry axis follows the Boltzmann equation, as indicated in Eq. (14).

ly from shape. The average energies for  $\phi=90^\circ$  are smaller than those for  $\phi=0^\circ$  because the emission barriers are smaller along the long axis of the nucleus (specifically oriented at  $\phi=90^\circ$ ). The values of  $\tilde{l}_{rms}$  for  $\phi=0^\circ$  are somewhat larger than those for  $\phi=90^\circ$  because the average of  $R^2$  is larger if one views the nucleus along its short axis [Eq. (22)]. Similarly (for  $J_0=0$ ), the anisotropy  $W(90^\circ)/W(0^\circ)$  is due completely to the lower Coulomb barrier along the long axis.

As we increase the emitter spin  $J_0$ , the preferential emission at  $\phi=90^\circ$  is enhanced in much the same way as for spherical systems [Eqs. (20)–(27)]. The average energies [Eqs. (26) and (27)] and  $\tilde{l}_{rms}$  values [Eq. (22)] increase with spin for  $\phi=90^\circ$  due to the spinoff effect. (There is actually a small decrease of  $\langle \epsilon \rangle_{\phi=0^\circ}$  and  $\tilde{l}_{rms\phi=0^\circ}$  due to the decrease of temperature with increasing spin and rotational energy.) Of greater interest is the important change in balance between the Coulomb and the spinoff effect (on  $\langle \epsilon \rangle$  and  $\tilde{l}_{rms}$  for  $\phi=90^\circ$ ) for the heavy system [Fig. 6(a)] compared to the lighter one [Fig. 6(b)]. This is due to the relative magnitudes of the emission barriers and the moments of inertia [note that  $\beta_2 \propto \mathcal{I}_d^{-1}$  in Eq. (21)].

In Fig. 7 we show results for the same reactions, but now we allow for a distribution of  $\phi^*$  as described by  $\tilde{P}_k(\phi^*)$  in Eq. (14). In this situation the differences between  $\phi=0^\circ$  and  $\phi=90^\circ$  are greatly reduced due to the spread of orientations about  $\phi^*=90^\circ$  for the prolate shape and about  $\phi^*=0^\circ$  for the oblate shape. For small spins the width of the  $\phi^*$  distribution is very large, but for large spins it becomes rather narrow. Next, we discuss results (Fig. 8) for the heavy system with  $J_0=67\hbar$  and for the light system with  $J_0=30\hbar$ . It is important to note (Figs.

6 and 7) that for the former there is very little influence from spinoff effects at  $J_0=67\hbar$ , while for the latter there is a very strong influence of spinoff effects for  $J_0=30\hbar$ .

In Fig. 8 we show, for fixed spin, the effect of shape on the same average properties. For the spherical shape, the changes between  $\phi=0^\circ$  and  $\phi=90^\circ$  arise solely from spinoff effects. Clearly, these effects are very small in Fig. 8(a) and very large in Fig. 8(b). As we increase the deformation,  $\tilde{\epsilon}$ , the average energy at  $\phi=90^\circ$  is reduced. This decrease results from the combined effects of lower average emission barriers and smaller spinoff energies due to an increase in the moment of inertia ( $\mathcal{I}_1$ ).

For both  $\tilde{l}_{rms}$  and  $W(90^\circ)/W(0^\circ)$  we see an interesting contrast in the effect of deformation. For the heavy system [Fig. 8(a)], the spinoff effect is very weak, and the anisotropy [ $W(90^\circ)/W(0^\circ)$  increases with deformation due to the lowering of the emission barrier along the long axis (or towards  $\phi=90^\circ$ )]. Similarly, the values of  $\tilde{l}_{rms\phi=90^\circ}$  are essentially constant while  $\tilde{l}_{rms\phi=0^\circ}$  increases slightly with deformation. By contrast, for the light system (Fig. 8(b)), the spinoff effect is very strong, and the values of both  $W(90^\circ)/W(0^\circ)$  and  $\tilde{l}_{rms\phi=90^\circ}$  decrease with deformation due to the increasing moment of inertia ( $\mathcal{I}_1$ ) and the associated decrease of the spinoff effect. These two cases illustrate the limiting situations discussed by Dossing<sup>15</sup> for the dominance of Coulomb forces [Fig. 8(a)] or centrifugal forces [Fig. 8(b)].

In Fig. 9 we show, for fixed spin, a second study of the effect of shape. Here we compare oblate and pear shapes to the spherical and prolate forms in Fig. 8. The average energies  $\langle \epsilon \rangle$  follow rather similar trends for the two systems. The spinoff enhancement in Fig. 9(a) is almost negligible for  $\langle \epsilon \rangle_{\phi=90^\circ}$ , but it is quite large in Fig. 9(b). The contrasting results for  $\tilde{l}_{rms}$  and  $W(90^\circ)/W(0^\circ)$  are very clear in Fig. 9, just as in Fig. 7 above.

In Figs. 10(a), 11(a), and 12(a) we show calculated results (for ideal coincidence experiments) with three additional reaction systems. The reaction 1080 MeV  $^{40}\text{Ar} + ^{238}\text{U}$  (Fig. 10) is distinguished by its very high temperature, near the limit for energy containment in a composite nucleus.<sup>26</sup> The rotating liquid drop model (RLDM) gives no equilibrium shapes for this system; therefore, any evaporative emission from the composite nuclei should occur along the dynamical path toward “fast-fission.” The reaction 340 MeV  $^{40}\text{Ar} + ^{108}\text{Ag}$  (Fig. 11) is of particular interest due to the roughly equal amounts of fusion fission and evaporation residue (ER) formation.<sup>27</sup> The RLDM predicts a driving force toward oblate shapes for the lower-spin zone [(0–72) $\hbar$ ] that leads to ER’s.<sup>5</sup> The higher-spin zone [(72–103) $\hbar$ ] that leads to fission should be driven toward prolate shapes. This higher-spin group should be divided between dynamical paths that must surmount a fission barrier and “fast-fission” paths that have little or no barrier. Quite different dynamical shapes might thus be expected for reactions leading to ER’s and to fission. For both of the cases shown in Figs. 10 and 11, the effects of Coulomb and centrifugal forces are important, but neither is completely dominant.

The reaction 140 MeV  $^{16}\text{O} + ^{27}\text{Al}$  (Fig. 12) is particularly interesting because of the exceptionally strong domi-

nance of spinoff effects. This dominance can be related, in part, to the mass factors  $\mu R^2/(\mathcal{I}_d + \mu R^2)$  and  $\mathcal{I}_d/(\mathcal{I}_d + \mu R^2)$  in Eqs. (21)–(27). For heavy systems the first factor is very small and the latter factor is almost unity. For this reaction both factors are  $\approx \frac{1}{2}$ , and this leads to a very large value of  $\beta_2$  and hence to very large spinoff

effects. Figure 12(a) shows these effects very clearly in the anisotropies and in the differences between  $\langle \epsilon \rangle_{\phi=0^\circ}$  and  $\langle \epsilon \rangle_{\phi=90^\circ}$ .

Each of these reactions (Figs. 10–12) has a particular character, and it will be interesting to see if the role of shape can be identified and, indeed, if the effective shapes

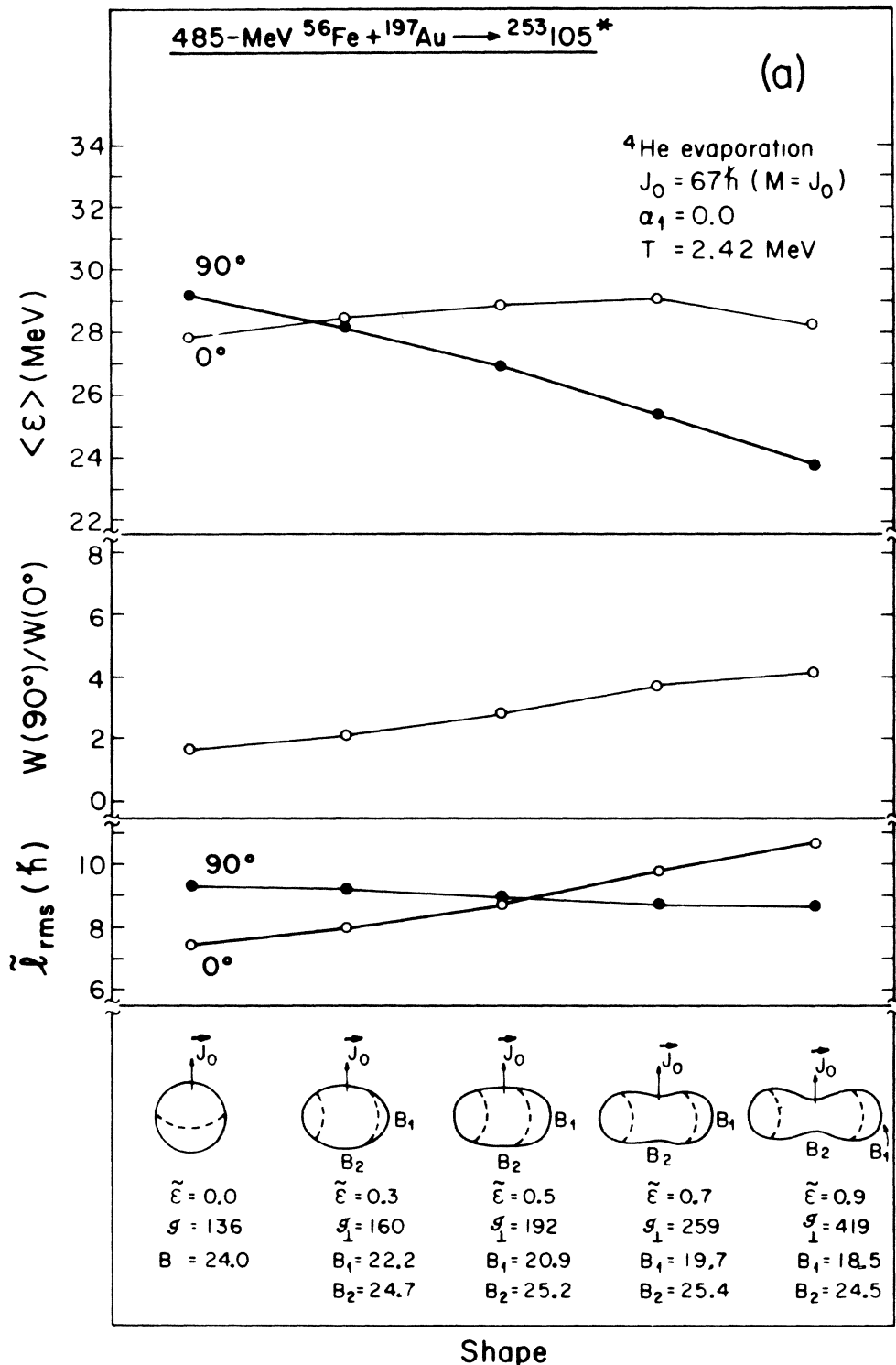


FIG. 8. Dependence on deformation (near prolate shapes) for certain average quantities. (a) 485 MeV  $^{56}\text{Fe} + ^{197}\text{Au} \rightarrow ^{253}105^*$  ( $T=2.4$  MeV,  $J_0=67\hbar$ ,  $\beta_{2,\text{sphere}}=0.61$ ). (b) 190 MeV  $^{40}\text{Ar} + ^{27}\text{Al} \rightarrow ^{67}\text{Ga}^*$  ( $T=2.9$  MeV,  $J_0=30\hbar$ ,  $\beta_{2,\text{sphere}}=4.0$ ). The units of  $B$  and  $\mathcal{I}$  are MeV and  $\hbar^2 \text{MeV}^{-1}$ , respectively.

can be determined.

For actual experimental measurements it is never possible to achieve the ideal situation of perfect alignment as discussed above. It is beyond the scope of this paper to cover the extent of alignment that can be realized by various coincidence requirements (e.g., with fission frag-

ments,<sup>24</sup>  $\gamma$  rays,<sup>28</sup> other light particles,<sup>29</sup> etc.) Nevertheless, it is clear that, as the degree of alignment is reduced, the observable effects will be reduced by the averaging over the orientation angle for  $J_0$ .<sup>15,25</sup> A commonly encountered situation is for  $J_0$  to be uniformly distributed in a plane perpendicular to the beam (i.e.,  $M=0$ ). This

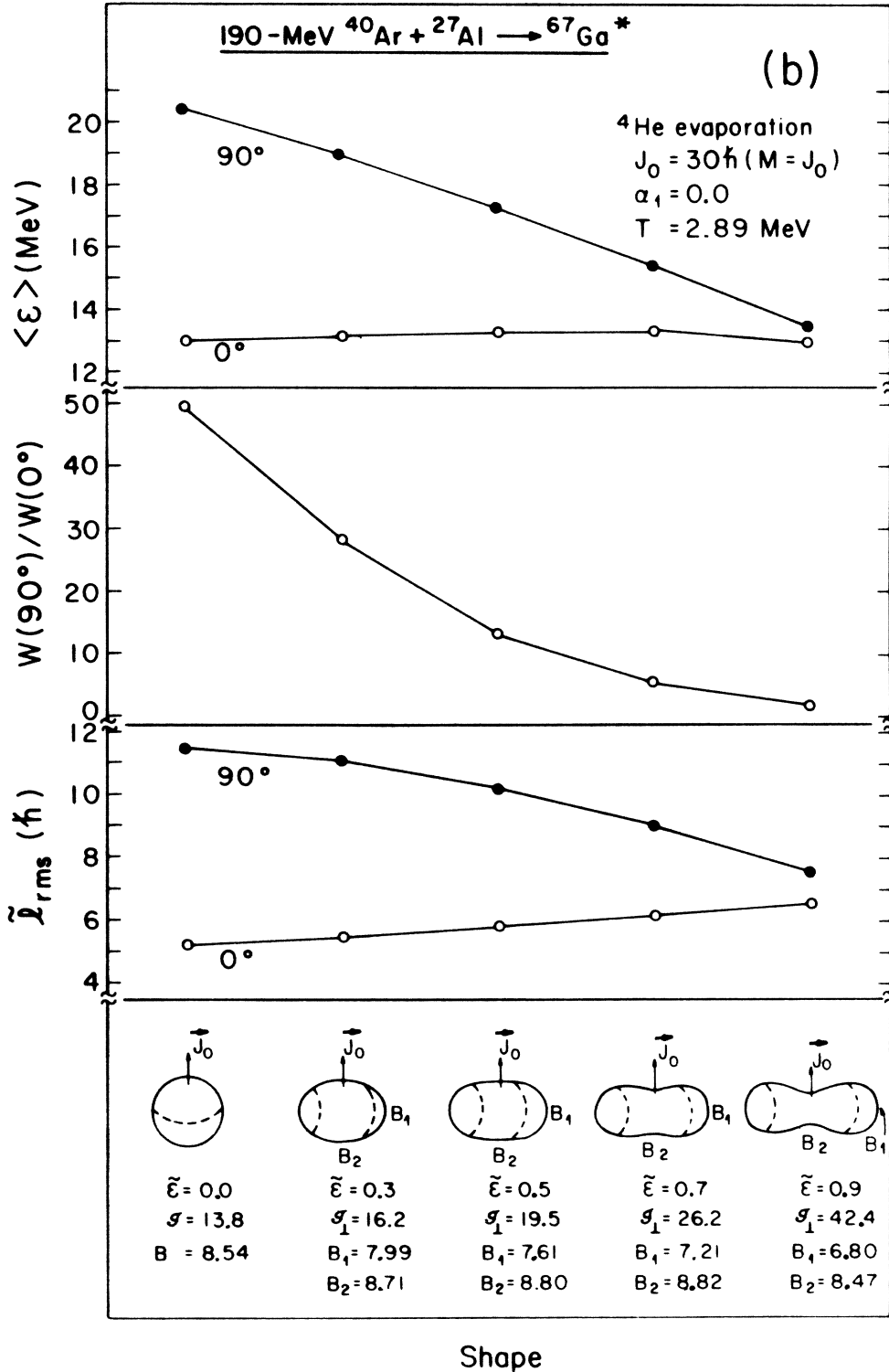


FIG. 8. (Continued).

geometrical description is a good approximation for many inclusive experiments.<sup>17,30</sup>

In Figs. 10(b), 11(b), and 12(b) we give calculated results for such singles experiments. All the trends in Figs. 6–9, 10(a), 11(a), and 12(a) are still present, but the magnitudes are greatly reduced. In each case the mean energies for

$\phi=90^\circ$  ( $M=J$ ) must be equal to those for  $\theta=0^\circ$  ( $M=0$ ); geometrically, they are equivalent, since for  $\theta=0^\circ$  all values of  $\phi$  are  $90^\circ$ . By contrast, for  $\theta=90^\circ$  ( $M=0$ ) the geometry averages over all spin directions from  $\phi=0^\circ$  to  $\theta=90^\circ$ . In the case of Fig. 12, where the anisotropy is extremely large (strong preference for  $\phi=90^\circ$ ), the mean en-

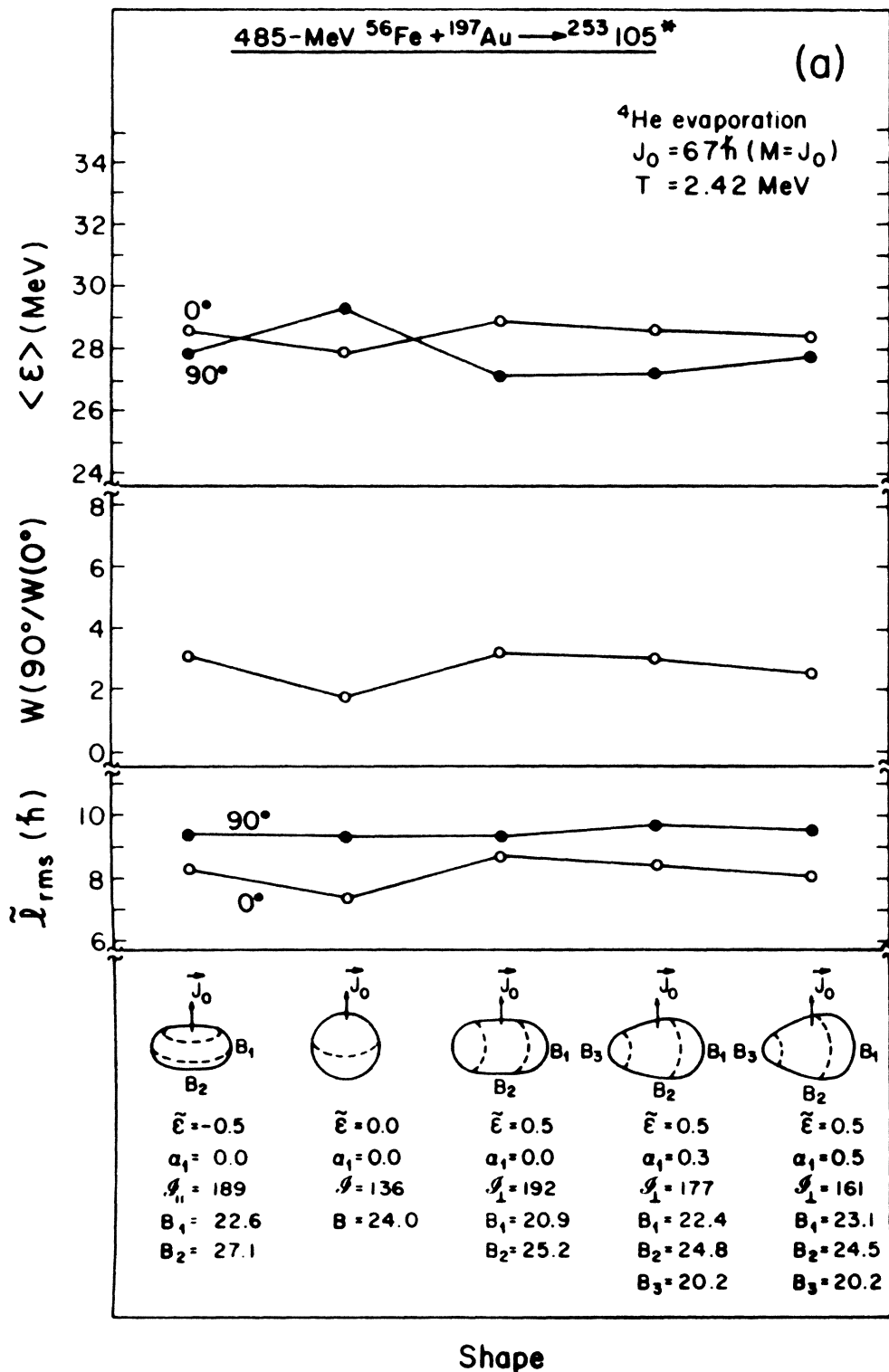
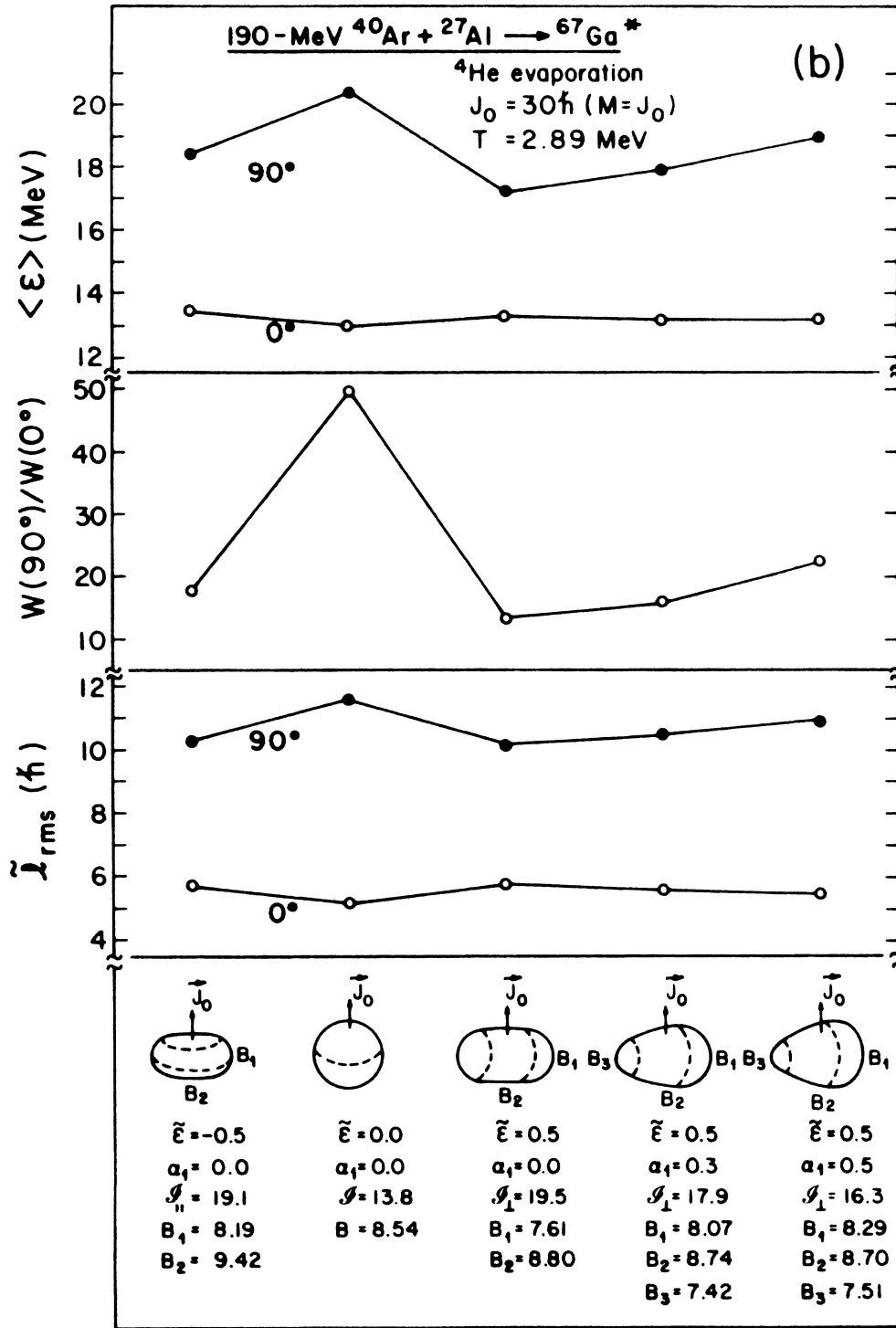


FIG. 9. Same as Fig. 8, but for oblate, spherical, prolate, and pear shapes.

ergies in singles, even at  $\theta=90^\circ$ , are very close to those for  $\theta=0^\circ$  (or  $\phi=90^\circ$ ). However, for the cases shown in Figs. 10(b) and 11(b) the mean energies in singles at  $\theta=90^\circ$  are closer to the average of those for  $\phi=0^\circ$  and  $90^\circ$ . This difference is due to the strength of the weighting from the angular distribution.

We conclude that singles data can be very useful, but that the sensitivity of the probe can be strongly enhanced by achieving some degree of alignment. In the GANES program we have provided several options to simulate various coincidence triggers and their expected effects for spin alignment. As these situations are quite varied, they



**Shape**

FIG. 9. (Continued).

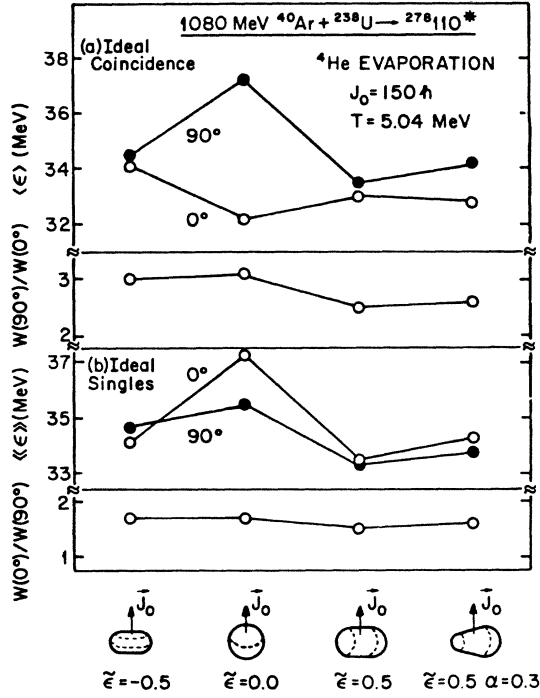


FIG. 10. Dependence on shape of certain average quantities. 1080 MeV  $^{40}\text{Ar} + ^{238}\text{U} \rightarrow ^{278}\text{X}^*$  ( $T = 5.0$  MeV,  $J_0 = 150\hbar$ ,  $\beta_{2,\text{sphere}} = 1.1$ ). (a) Ideal coincidence experiments. (b) Ideal singles experiments.

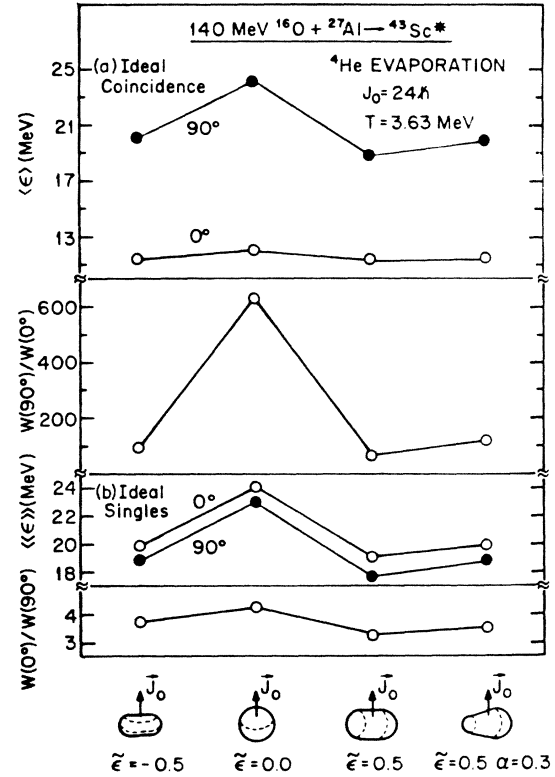


FIG. 12. Dependence on shape of certain average quantities. 140 MeV  $^{16}\text{O} + ^{27}\text{Al} \rightarrow ^{43}\text{Sc}^*$  ( $T = 3.8$  MeV,  $J_0 = 24\hbar$ ,  $\beta_{2,\text{sphere}} = 6.2$ ). (a) Ideal coincidence experiments. (b) Ideal singles experiments.

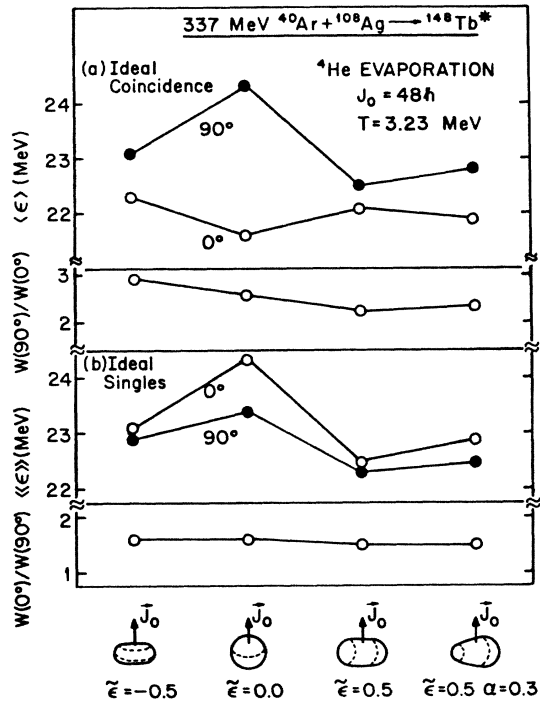


FIG. 11. Dependence on shape of certain average quantities. 334 MeV  $^{40}\text{Ar} + ^{108}\text{Ag} \rightarrow ^{148}\text{Tb}^*$  ( $T = 3.2$  MeV,  $J_0 = 48\hbar$ ,  $\beta_{2,\text{sphere}} = 1.2$ ). (a) Ideal coincidence experiments. (b) Ideal singles experiments.

are best discussed individually in the context of each particular experiment.

The major conclusion that we draw here is that the shape of the nuclear system can be expected to cause readily observable effects on evaporative  $^4\text{He}$  emission. The degree to which these effects can be identified depends on the extent and detail of the combined experimental and theoretical attack and, in particular, on the power of the coincidence trigger. Several high-quality experiments have already been performed and others are in progress (see, for example, Refs. 24–31).

## VII. SUMMARY

We have described a method for calculating evaporation spectra and angular distributions for deformed nuclear systems. The semiclassical approach follows very closely the widely used Ericson formulation for spheres.<sup>9</sup> A Monte Carlo technique has been employed in the framework of the well documented computer code GANES.<sup>16</sup> The calculated results indicate that effects due to differences in nuclear shapes are large enough to be observed, especially for carefully executed coincidence experiments. These results provide encouragement that evaporative particle emission contains important clues to the shapes of very hot nuclei.

- <sup>1</sup>A. Bohr and B. Mottelson, *Nuclear Structure* (Benjamin, New York, 1975), Vol. 2, p. 607.
- <sup>2</sup>S. Bjornholm and W. J. Swiatecki, *Nucl. Phys.* **A391**, 471 (1982).
- <sup>3</sup>T. Dossing and J. Randrup, *Nucl. Phys.* **A433**, 215 (1985); **A433**, 280 (1985).
- <sup>4</sup>P. Grange, Li Jun-Qing, and H. A. Weidenmuller, *Phys. Rev. C* **27**, 2063 (1983).
- <sup>5</sup>S. Cohen, F. Plasil, and W. J. Swiatecki, *Ann. Phys. (N.Y.)* **82**, 557 (1974); M. G. Mustafa, P. A. Baisden, and H. Chandra, *Phys. Rev. C* **25**, 2524 (1982).
- <sup>6</sup>M. Blann and T. T. Komoto, *Phys. Rev. C* **24**, 426 (1981).
- <sup>7</sup>H. Delagrange, C. Gregoire, F. Schleuter, and Y. Abe, *Z. Phys. A* **323**, 437 (1986).
- <sup>8</sup>H. Feldmeier and H. Spangenberg, *Nucl. Phys.* **A428**, 223c (1984).
- <sup>9</sup>T. Ericson, *Adv. Phys.* **9**, 425 (1960).
- <sup>10</sup>C. K. Gelbke, *Commun. Nucl. Part. Phys.* **11**, 259 (1983).
- <sup>11</sup>L. C. Vaz, D. Logan, E. Duek, J. M. Alexander, M. F. Rivet, M. S. Zisman, M. Kaplan, and J. W. Ball, *Z. Phys. A* **315**, 169 (1984), and references therein.
- <sup>12</sup>R. Freifelder, M. Prakash, and J. M. Alexander, *Phys. Rep.* **133**, 315 (1986).
- <sup>13</sup>J. M. Alexander, Daniel Guerreau, and L. V. Vaz, *Z. Phys. A* **305**, 313 (1982).
- <sup>14</sup>V. V. Pashkevich, *Nucl. Phys.* **A169**, 275 (1971).
- <sup>15</sup>T. Dossing, Licentiat thesis, University of Copenhagen, 1977.
- <sup>16</sup>N. N. Ajitanand, R. Lacey, G. F. Peaslee, E. Duek, and J. M. Alexander, *Nucl. Instrum. Methods Phys. Res. A* **243**, 111 (1986).
- <sup>17</sup>A start in this direction is reported by D. J. Moses, M. Kaplan, J. M. Alexander, D. Logan, M. Kildir, Louis C. Vaz, N. N. Ajitanand, E. Duek, and M. S. Zisman, *Z. Phys. A* **320**, 229 (1985).
- <sup>18</sup>T. Ericson and V. Strutinski, *Nucl. Phys.* **8**, 284 (1958).
- <sup>19</sup>E. D. Cashwell and C. J. Everett, *A Practical Manual on the Monte Carlo Method for Random Walk Problems* (Pergamon, New York, 1959).
- <sup>20</sup>N. Carjan and B. Leroux, *Phys. Rev. C* **22**, 2008 (1981).
- <sup>21</sup>Louis C. Vaz and J. M. Alexander, *Z. Phys. A* **318**, 231 (1984).
- <sup>22</sup>D. L. Hill and J. A. Wheeler, *Phys. Rev.* **89**, 1102 (1953).
- <sup>23</sup>L. C. Vaz, J. M. Alexander, and N. Carjan, *Z. Phys. A* (in press).
- <sup>24</sup>M. F. Rivet, D. Logan, J. M. Alexander, D. Guerreau, E. Duek, M. S. Zisman, and M. Kaplan, *Phys. Rev. C* **25**, 2430 (1982).
- <sup>25</sup>G. L. Catchen, M. Kaplan, J. M. Alexander, and M. F. Rivet, *Phys. Rev. C* **21**, 940 (1980).
- <sup>26</sup>D. Jacquet, E. Duek, J. M. Alexander, B. Borderie, J. Galin, D. Gardes, D. Gurreau, M. Lefort, F. Monnet, M. F. Rivet, and X. Tarrago, *Phys. Rev. Lett.* **53**, 2226 (1984).
- <sup>27</sup>N. N. Ajitanand, J. M. Alexander, H. Delagrange, E. Duek, D. O. Eriksen, D. Guerreau, M. Kaplan, M. Kildir, L. Kowalski, R. Lacey, D. Logan, D. J. Moses, G. F. Peaslee, L. C. Vaz, and M. S. Zisman, *Z. Phys. A* **316**, 169 (1984).
- <sup>28</sup>F. A. Dilmanian, D. G. Sarantites, M. Jaaskelainen, H. Puchta, R. Woodward, J. R. Beene, D. C. Hensley, M. L. Halbert, R. Novotny, L. Adler, R. K. Choudhury, M. N. Namboodiri, R. P. Schmitt, and J. B. Natowitz, *Phys. Rev. Lett.* **49**, 1909 (1982).
- <sup>29</sup>T. Kuang-Hsi, T. Dossing, C. Gaarde, and J. S. Larsen, *Nucl. Phys.* **316**, 189 (1979).
- <sup>30</sup>R. C. Reedy, M. J. Fluss, G. F. Herzog, L. Kowalski, and J. M. Miller, *Phys. Rev.* **188**, 1771 (1969); J. Galin, B. Gatty, D. Guerreau, C. Rousset, U. C. Schlotthauer-Voos, and X. Tarrago, *Phys. Rev. C* **9**, 1113 (1974); J. Galin, B. Gatty, D. Guerreau, C. Rousset, U. C. Schlotthauer-Voos, and X. Tarrago, *ibid.* **9**, 1126 (1974).
- <sup>31</sup>L. Schad, H. Ho, G.-Y. Fan, B. Lindl, A. Pfoh, R. Wolski, and J. P. Wurm, *Z. Phys. A* **318**, 179 (1984).